

Enhancing operational stability of OLEDs based on subatomic modified thermally activated delayed fluorescence compounds

Received: 1 July 2023

Accepted: 26 September 2023

Published online: 14 October 2023

 Check for updates

Sinyeong Jung^{1,2,6}, Wai-Lung Cheung^{1,6}, Si-jie Li^{1,6}, Min Wang¹, Wansi Li¹, Cangyu Wang¹, Xiaoge Song¹, Guodan Wei^{1,2}✉, Qinghua Song¹, Season Si Chen³✉, Wanqing Cai⁴, Maggie Ng¹, Wai Kit Tang⁵ & Man-Chung Tang¹✉

The realization of operationally stable blue organic light-emitting diodes is a challenging issue across the field. While device optimization has been a focus to effectively prolong device lifetime, strategies based on molecular engineering of chemical structures, particularly at the subatomic level, remains little. Herein, we explore the effect of targeted deuteration on donor and/or acceptor units of thermally activated delayed fluorescence emitters and investigate the structure-property relationship between intrinsic molecular stability, based on isotopic effect, and device operational stability. We show that the deuteration of the acceptor unit is critical to enhance the photostability of thermally activated delayed fluorescence compounds and hence device lifetime in addition to that of the donor units, which is commonly neglected due to the limited availability and synthetic complexity of deuterated acceptors. Based on these isotopic analogues, we observe a gradual increase in the device operational stability and achieve the long-lifetime time to 90% of the initial luminance of 23.4 h at the luminance of 1000 cd m⁻² for thermally activated delayed fluorescence-sensitized organic light-emitting diodes. We anticipate our strategic deuteration approach provides insights and demonstrates the importance on structural modification materials at a subatomic level towards prolonging the device operational stability.

To realize blue organic light-emitting diodes (OLEDs) with high efficiency and long operational lifetime, it is important to suppress bimolecular triplet-triplet annihilation (TTA) or and triplet-polaron annihilation (TPA) which could induce undesirable exciton fusion processes such as high-energy polaron formation^{1,2}. For example, the employment of a stacked device structure with two emissive layers (EMLs) with graded dopant concentrations³, the introduction of an

excited state manager molecule as a sacrificing agent⁴, and the use of sky-blue thermally activated delayed fluorescence (TADF) emitters as assistant dopants⁵ have been shown to effectively lengthen the device lifetime. While intensive efforts have been made in terms of device engineering⁶, there has been a recent interest on molecular engineering to investigate the structure-property relationship with strategies that pinpoint on the emitter or host material design from a

¹Institute of Materials Research, Tsinghua Shenzhen International Graduate School, Tsinghua University, 518055 Shenzhen, China. ²Tsinghua-Berkeley Shenzhen Institute (TBSI), Tsinghua University, 518055 Shenzhen, China. ³Institute of Environment and Ecology, Tsinghua Shenzhen International Graduate School, Tsinghua University, 518005 Shenzhen, China. ⁴Faculty of Materials Science, MSU-BIT University, 518172 Shenzhen, China. ⁵Department of Chemistry, Faculty of Science, University of Malaya, 50603 Kuala Lumpur, Malaysia. ⁶These authors contributed equally: Sinyeong Jung, Wai-Lung Cheung, Si-jie Li ✉ e-mail: weiguodan@sz.tsinghua.edu.cn; season.chen@sz.tsinghua.edu.cn; kobetang2021@sz.tsinghua.edu.cn

chemical point of view^{7,8}, which are of equal importance to enhance the device operational lifetime. Specifically, a particular focus has been put on the exploration of factors such as the bond dissociation energy (BDE) of host materials⁹ and deuterium substitution of host materials^{10–12}, phosphorescent (Ph) emitters^{13–18} or donor units of TADF emitters^{19,20}. These have prompted our interest to take a deeper investigation on the isotopic effect induced by different components within the material on the device operational stability.

The kinetic isotopic effect (KIE) is a mechanistic phenomenon associated with one of the atoms being replaced by its isotope with the observation of a change of rate of a chemical reaction²¹. Among various isotopic effect, the replacement of proton, or protium, by deuterium is the most common strategy considering the relative ease and cost of synthesis, as well as the more prominent effect based on the change of mass, compared to other isotope effects such as carbon-13²². For hydrogen isotopic effect, it is often expressed by the ratio of k_H/k_D in the range of 1–7 depending on the site of substitution, where primary hydrogen KIE refers to the substitution at the bond breaking site and secondary hydrogen KIE refers to the substitution other than the bond breaking site in the rate determining step. According to Eq. (1),

$$\nu = \frac{1}{2\pi} \sqrt{\frac{k}{\mu}} \quad (1)$$

where ν is the vibration frequency, k is the force constant, and μ is the reduced mass, the substitution of an atom by its heavier isotope requires a higher activation energy for bond dissociation. Therefore, it is anticipated that deuterium substitution could enhance the intrinsic stability of a molecule. This has been evidenced by a lower vibrational zero point energy (ZPE) of deuterated polymers²³ and an increased photoluminescence quantum yield (PLQY) of near-infrared emitters owing to the lower non-radiative decay rate (k_{nr}) through a reduced reorganization energy (λ) and exciton-vibration coupling (i.e. a smaller Franck–Condon factor (F))¹⁷. To date, only few research has been reported to study the improved molecular stability through deuterium substitution in OLED applications^{11,12,20}. For instance, Adachi and co-workers reported a host material with deuterated carbazole donors

that exhibited a 2-fold enhancement of device half lifetime, i.e. LT_{50} at an initial luminance of 1000 cd m^{-2} , from 17 h to 40 h compared to its non-deuterated counterpart¹¹; while the isotopic effect has been shown positive on the thermal stability and electroluminescence (EL) of TADF emitters²⁰, the underlying mechanism of such effect has not yet been studied in correlation with the corresponding device operational stability. More importantly, to the best of our knowledge, studies on deuterated single emitting materials are solely based on donor units of TADF compounds^{19,20,24}, or random deuteration of host materials¹², suggesting the capacity of fully deuterated materials, as well as the position and degree of deuteration of different components of a molecule with respect to the distances to potential bond breaking sites, e.g. C–N bond^{25,26}, has yet to be unlocked.

In light of these, our interest focuses on the investigation of the isotopic effect through independent deuteration of the donor and acceptor units. We take advantage of the symmetrical, robust and rigid oxygen-bridged triarylboron unit^{27,28} to study such effect in a series of deuterated isotopic analogues, with a targeted deuteration of diphenylamine (DPA) and/or phenoxy groups on the 5,9-dioxa-13b-bor-anaphtho[3,2,1-de]anthracene (BO) moieties, namely DPA-BO, d-DPA-BO, DPA-d-BO and d-DPA-d-BO (Fig. 1a). We conduct a comprehensive study on the deuterated effect towards their photophysical behavior, intrinsic stability and device operational lifetime. Under the irradiation of a high-power lamp, we found that the photostability of the compounds increases with the degree of deuteration as observed from the time-dependent UV-vis and PL spectra in solution, neat film and doped film, supported by theoretical studies where the increased BDE of the C–D bond imposes an additive effect on the molecules. These results suggest the important role of deuterated acceptor unit that is critical to enhance the overall stability of the compounds, which is commonly neglected due to their limited commercial availability and synthetic difficulty. Based on this series of compounds, we observe a gradual increase in the device operational stability and achieve the LT_{90} of 23.4 h at the luminance of 1000 cd m^{-2} for TADF-sensitized OLEDs. We hope that the present study provides insights into further boosting the device operational stability through the strategic deuteration of luminescent compounds at the subatomic level.

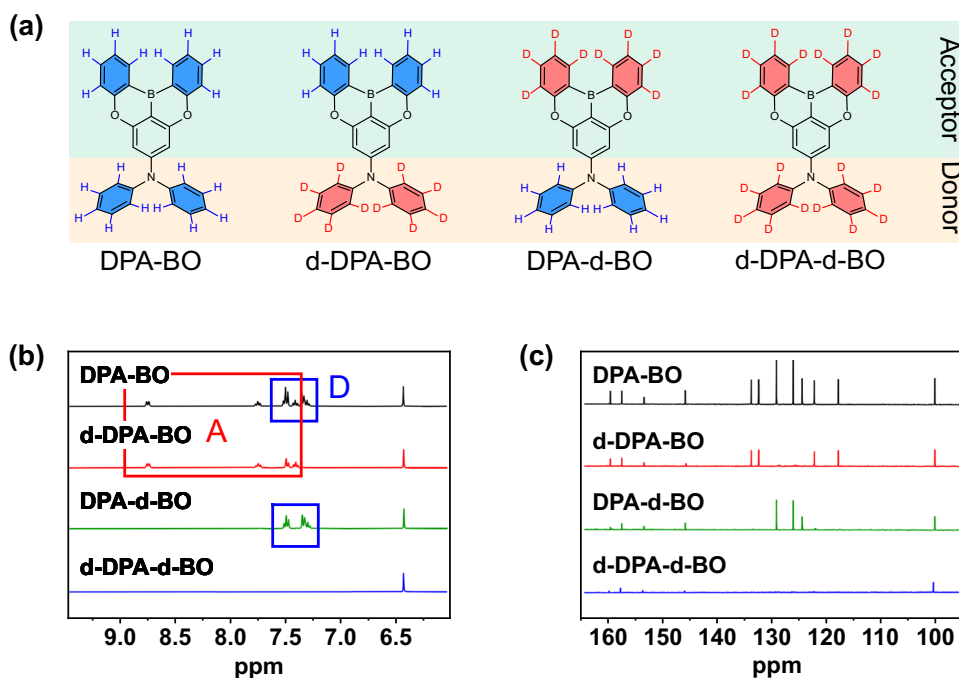


Fig. 1 | Molecular structures and characterization of synthesized compounds. a Chemical structures of the investigated TADF emitters. **b** ¹H NMR stacked spectra. **c** ¹³C NMR stacked spectra.

Results

Synthesis and characterization

Supplementary Fig. 1–3 illustrate the synthetic route for precursor compounds BO, d-BO, and d-DPA. The series of deuterated isotopic analogues was synthesized by Buchwald–Hartwig coupling reaction, as shown in Supplementary Fig. 4, and well-characterized by ^1H and $^{13}\text{C}\{^1\text{H}\}$ nuclear magnetic resonance spectroscopy and high-resolution electrospray ionization mass spectrometry (Supplementary Fig. 5–21). As expected, the proton signals of d-BO and d-DPA moieties are not found in respective compounds, while a singlet peak centered at 6.52 ppm exists in all compounds which belongs to the protons on the central aromatic ring (Fig. 1b). In addition, we have also observed the peaks corresponding to the carbon atom bonded with deuterium showing a weaker signal in the ^{13}C -NMR spectra (Fig. 1c), possibly attributed to the different magnetic moment of proton and deuterium. Meanwhile, we observe a concomitantly drop in the absorption peak at ca. 3040 cm^{-1} and emergence of the peak at ca. 2280 cm^{-1} in the infrared (IR) spectra upon increasing the degree of deuteration, corresponding to the C–H and C–D bond stretches, respectively (Supplementary Fig. 22a). These results are in good agreement with the simulated IR spectra of the compounds (Supplementary Fig. 22b). The TADF compounds also show high decomposition (T_d) and glass transition (T_g) temperatures of over 340°C and 240°C , respectively (Supplementary Fig. 23 and Supplementary Table 1), proving to be thermally stable enough to be applied as emissive dopants in vacuum-deposited OLEDs.

Theoretical investigation

To gain insights into the nature of the absorption and emission origins, the excited states involved in the TADF process, density functional theory (DFT) and time-dependent density functional theory (TDDFT) calculations were performed on these compounds. The spatial plots of the highest occupied molecular orbital (HOMO) and lowest unoccupied molecular orbital (LUMO) of representative

compound DPA-BO at the optimized ground-state geometry are shown in Fig. 2, while those of other selected molecular orbitals are illustrated in Supplementary Fig. 24–27. Apparently, the HOMOs of these compounds are predominantly the π -orbitals localized on the DPA moiety, while the LUMOs are predominantly the π^* orbitals localized on the BO moiety. Based on the simulated absorption spectra of all compounds, as shown in Supplementary Fig. 28, and their first fifteen singlet excited states listed in Supplementary Table 2, we assign the low-energy absorption band to be originating from the S_1 state with charge-transfer (CT) character from the DPA moiety to BO moiety. The emission energies of the S_1 state are estimated to be ca. 408 nm (Supplementary Table 3). Supplementary Fig. 29–31 illustrate the selected molecular orbitals of DPA-BO at the optimized S_1 , T_1 , and T_2 states geometry. Apparently, the S_1 and T_1 states are of the CT character (^1CT and ^3CT , respectively) while the T_2 state is of the localized state character (^3LE). The computed energy differences between the S_1 and T_1 states, i.e. $\Delta E(S_1-T_1)$, and that between the S_1 and T_2 states, i.e. $\Delta E(T_2-S_1)$, are found to be 0.22 eV and 0.08 eV, respectively. Meanwhile, the computed values of the spin-orbit coupling (SOC) matrix elements²⁹, $\langle ^1\text{CT} | \hat{H}_{\text{SOC}} | ^3\text{CT} \rangle$ and $\langle ^1\text{CT} | \hat{H}_{\text{SOC}} | ^3\text{LE} \rangle$, are found to be 0.150 cm^{-1} and 0.103 cm^{-1} , respectively. Although heavy atom could improve the SOC, the same estimated SOC constants for all compounds also imply an insignificant impact on the SOC upon deuteration of the compounds²⁰.

To estimate the effect of deuteration, we compute the ZPE, and the BDE of C–H (or C–D) bond at ground-state geometry as well as C–N bond between donor and acceptor units, of the compounds at the S_0 and T_1 states. The ZPE of these compounds and DPA and BO precursor compounds are listed in Supplementary Table 4, whereas the BDE of the C–N bond and the C–H (or C–D) bond are summarized in Supplementary Tables 5, 6. Regarding the C–N bond dissociation, the ZPE decreases from $262.9\text{ kcal mol}^{-1}$ to $226.1\text{ kcal mol}^{-1}$ upon increasing the degree of deuteration in general (Supplementary Table 4). It should be

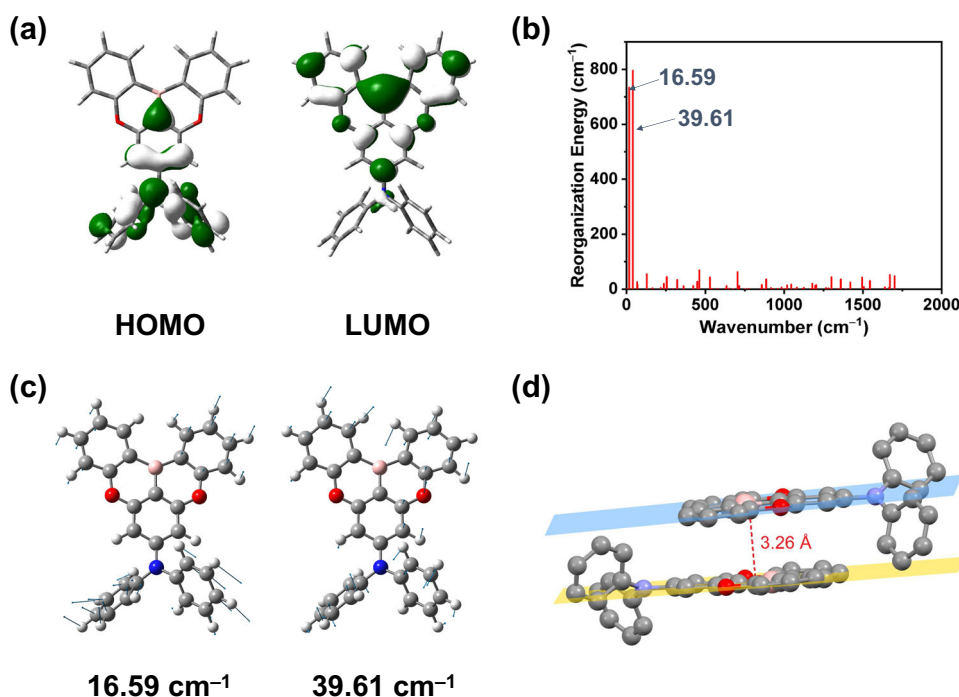


Fig. 2 | Theoretical investigation of the deuterated isotopologues. **a** Spatial plots (isovalue = 0.03) of the HOMO and LUMO for the selective compound DPA-BO at the optimized ground-state geometry. **b** Plots of computed reorganization energies as a function of normal mode wavenumbers for S_1 - S_0 of DPA-BO.

c Illustration of selected normal modes contributing to large reorganization energies for the S_0 state of DPA-BO. **d** Ground-state geometry of the dimer of DPA-BO optimized at the M06 level.

noted that the addition of ZPE values of DPA and BO precursor compounds are not equal to the ZPE of the final compounds. The BDE of the C–N bond at the S_0 state is found to drop slightly upon deuterating the compounds, whereas the values at the T_1 state do not show apparent changes and are ca. 0.66 eV. The transition states of the C–N bond dissociation of the T_1 state of DPA-BO and d-DPA-d-BO have been located and their enthalpies of activation are summarized in Supplementary Table 7. The enthalpies of activation are ca. 0.90 eV and they show insignificant difference upon deuteration. Therefore, from both the thermodynamic and kinetic aspects, deuteration of DPA-BO does not strengthen the C–N bond, nor does it influence the rate of C–N bond dissociation. On the other hand, the BDE of the C–D bond is higher than that of the C–H bond by ca. 0.1 eV. With multiple C–D bonds existing in the compounds (i.e. 10 in d-DPA-BO, 8 in DPA-d-BO; 18 in d-DPA-d-BO), the additive effect should be appreciable, and hence the proton abstraction reaction is thermodynamically less favorable and subsequent formation of high molecular adducts is probably suppressed^{12,30,31}. In short, upon deuteration of DPA-BO, though the C–N bond is slightly weakened, the strengthening of multiple C–D bonds in the compounds is suggested to prevent most of the proton abstraction reaction and subsequent radical formations. With these calculated results, we anticipate that the higher degree of deuteration on both donor and acceptor units should exert a more prominent effect on the device stability.

In addition, the effects of deuteration of the compounds on their Huang-Rhys factor (S_j), reorganization energy (λ_j), radiative (k_r) and nonradiative (k_{nr}) decay rate constants have been investigated. The plot of the computed λ_j as a function of normal mode wavenumbers of DPA-BO for S_1 - S_0 is shown in Fig. 2b, whereas those of other molecules are shown in Supplementary Fig. 32. It is obvious that the λ_j is contributed predominantly by the low-frequency vibrational modes under 50 cm^{-1} . The low-frequency vibrational modes of DPA-BO are illustrated in Fig. 2c and those of other molecules are shown in Supplementary Fig. 33 and 34. They are mainly the rotation of the phenyl rings in both the DPA and BO moieties, which contribute predominantly to the distortion of the S_1 geometry from the S_0 geometry. The displacement (ΔQ), Huang-Rhys factors (S_j) and reorganization energies of selected normal modes of the compounds are summarized in Supplementary Tables 8, 9, and the computed k_r and k_{nr} values are summarized in Supplementary Table 10. There is no obvious trend in ΔQ , S_j and λ_j upon the deuteration of the compounds, and the k_r ($1.18 \times 10^8 \text{ s}^{-1}$) and k_{nr} (ca. $1.4 \times 10^{11} \text{ s}^{-1}$) are nearly the same upon deuteration. Therefore, deuteration does not have significant effect on k_r and k_{nr} in this case, resemblance to our photophysical studies.

To further investigate the possible intermolecular interactions in the solid-state thin film, DFT calculation based on the dimer form of DPA-BO has been performed at the M06 level of theory. The optimized geometry of the dimer of DPA-BO is shown in Fig. 2d. The two planes of the BO moieties are nearly parallel and they are separated with a distance of 3.26 Å, which is within the separation between the π - π planes (ca. 3.35 Å), indicating the presence of π - π interactions in the solid-state thin film.

Photophysical and TADF properties

To well-characterize the electronic absorption, emissive and TADF properties of the deuterated isotopic analogues, we conduct steady-state UV-vis absorption and emission spectroscopy to study the photophysical behavior in both solution and solid-state thin film. Figure 3a shows the absorption and emission spectra of the compounds in degassed toluene and Supplementary Table 11 summarizes their photophysical data. In general, all compounds show moderate absorption bands at ca. 280–320 nm and intense absorption bands at 375 nm, attributing to the spin-allowed intraligand (IL) $\pi \rightarrow \pi^*$ transitions of the BO and DPA moieties and ligand-to-ligand charge transfer

(LLCT) [$\pi(\text{DPA}) \rightarrow \pi^*(\text{BO})$] transitions, respectively²⁸. Upon excitation at $\lambda \geq 340$ nm, all compounds feature a broad structureless fluorescence emission band with emission maxima peaking at 430 nm with a decay lifetime of ca. 4.4 ns, which is assigned as originating from the LLCT [$\pi(\text{DPA}) \rightarrow \pi^*(\text{BO})$] excited state. The effect of deuteration is found to be insignificant towards the photophysical properties of the TADF compounds, in agreement with the theoretical results. We also look into the solvent-dependent emission behavior considering the CT nature of the excited state of these compounds. Upon increasing the solvent polarity from cyclohexane to dichloromethane, we observe a bathochromic shift of the LLCT band maxima from ca. 400 nm to 470 nm (Supplementary Fig. 35), confirming the strong CT character of the emissive state.

Next, we study the photophysical and TADF properties of the compounds doped in bis[2-(diphenylphosphino)phenyl]ether oxide (DPEPO) thin films. Table 1 summarizes the TADF characteristics of the investigated compounds. The photoluminescence (PL) spectra recorded at room temperature for DPA-BO at 5–20 wt% are shown in Supplementary Fig. 36. It is clearly seen that the structureless blue emission band exhibits a bathochromic shift upon increasing the dopant concentration, suggesting a concentration-dependent behavior arising from π - π stacking of the BO moiety^{32,33}. This could be evidenced by the 3D images generated from time-of-flight secondary ion mass spectrometry (ToF-SIMS) which give information on the spatial localization of the host and emitting materials. Figure 3b shows the ToF-SIMS characteristics of the representative 10 wt% DPA-BO in DPEPO and those of the others are shown in Supplementary Fig. 37. In these images, we directly observe that the TADF compounds are not well-dispersed in the host matrix, indicating the presence of strong intermolecular interactions in the solid state, consistent with our computational results, which could possibly enhance the CT characteristics of the compounds³⁴. On the other hand, the PL transient emission spectra recorded at low temperature and the steady-state emission spectra at room temperature, representing the phosphorescence and fluorescence emission of the compounds doped at 10 wt% in DPEPO (Supplementary Fig. 38), where an estimated $\Delta E(S_1-T_1)$ of ca. 0.08 eV is found for all compounds. As shown in Fig. 3c, the transient PL decay curves of these compounds can be well-fitted by the biexponential model, in which the prompt and delayed lifetimes are found to be ca. 3.5 ns and 59–67 μs , respectively. We also analyze the temperature-dependency of k_{RISC} in 10 wt% of the compounds in DPEPO. Based on the Arrhenius Eq. (2):

$$k_{\text{RISC}} = A \exp(-E_a/k_{\text{BT}}) \quad (2)$$

where A is the frequency factor involving the SOC constant, E_a is the activation energy, and k_{BT} is the Boltzmann distribution, the estimated E_a values are in the range of 37–41 meV (Supplementary Fig. 39), much smaller than the activation energy needed for reverse intersystem crossing (RISC) at 300 K ($k_{\text{BT}} \approx 25.9$ meV). The HOMO and LUMO energies of these compounds, estimated by ultraviolet photoelectron spectroscopy (UPS) (Supplementary Fig. 40) and UV-vis spectroscopy, are also listed in Supplementary Table 11. These experimental results are generally in line with the theoretical studies. Based on the above theoretical and experimental results, we deduce that the small $\Delta E(S_1-T_2)$, together with the ineligible SOC constant²⁰, suggest possible RISC process from the T_2 to S_1 states^{35,36}. The schematic diagram of the energy levels and SOC matrix elements between the S_1 and T_n states are shown in Fig. 3d.

Intrinsic photostability

To investigate the effect of deuteration on the intrinsic photostability of the TADF compounds, we perform PL stability test on the compounds under a continuous irradiation with a CW ozone-free xenon arc lamp at room temperature. Supplementary Fig. 41 and 42 show

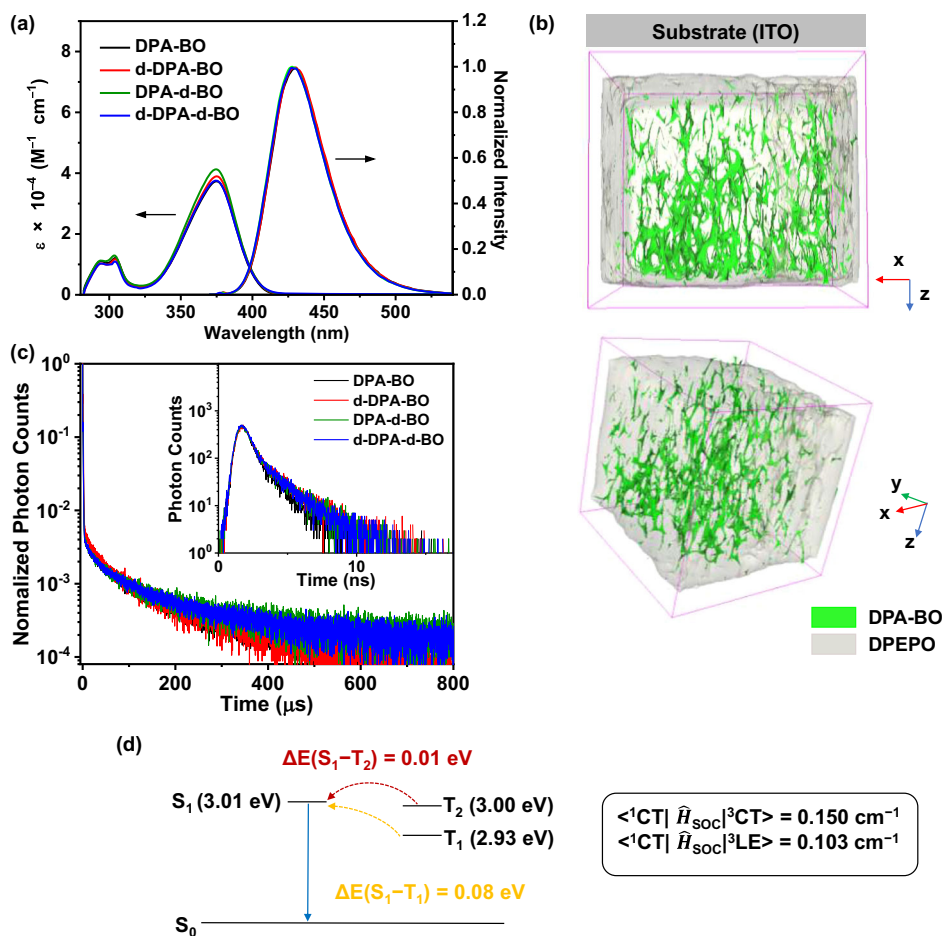


Fig. 3 | Photophysical properties and spatial localization in DPEPO film.

a UV-Vis and PL spectra recorded in toluene (2×10^{-5} M). **b** Spatial localization of 10 wt% DPA-BO ($C_{30}H_{28}BNO_2^+$, molar mass = 437.16 g/mol) doped in DPEPO

($C_{36}H_{28}O_3P_2^+$, molar mass = 570.09 g/mol). **c** Prompt (inset) and delayed PL decay of 10 wt% doped films. **d** Schematic diagram of the energy levels and SOC matrix elements between the S_1 and T_n states.

Table 1 | TADF characteristics of the investigated compounds

Compound	Φ_{PL} (%) ^a	Φ_p (%) ^b	Φ_d (%)	τ_p (ns)/ τ_d (μ s) ^c	k_{pf} (10^7 s ⁻¹) ^d	k_{df} (10^4 s ⁻¹) ^e	k_{ISC} (10^7 s ⁻¹) ^f	k_{RISC} (10^4 s ⁻¹) ^g
DPA-BO	89.0	68.9	20.0	3.5/67.2	19.6	0.3	4.4	0.4
d-DPA-BO	88.3	67.1	21.1	3.4/56.8	19.2	0.3	4.6	0.4
DPA-d-BO	89.3	63.9	25.4	3.4/64.1	18.7	0.4	5.3	0.6
d-DPA-d-BO	90.2	68.8	21.4	3.4/59.5	20.1	0.4	4.8	0.5

^aAbsolute PLQYs evaluated under N_2 of 10 wt% DPEPO thin film (298 K).

^bAbsolute PLQYs evaluated under air of 10 wt% DPEPO thin film (298 K).

^cPL lifetimes of prompt (τ_p) and delayed (τ_d) decay components in 10 wt% DPEPO thin film (298 K).

^d k_{pf} , prompt fluorescence rate constant⁵⁹.

^e k_{df} , delayed fluorescence rate constant⁵⁹.

^f k_{ISC} , intersystem crossing rate constant⁵⁹.

^g k_{RISC} , reverse intersystem crossing rate constant⁵⁹.

the UV-vis and PL spectra of the compounds in degassed toluene solution. Apparently, the shape of the absorption and emission bands remains unchanged, but the percentage of the CT absorption band at ca. 370 nm and the CT emission band at ca. 440 nm generally decreases to a lesser extent upon increasing the degree of deuteration, i.e., from 70.6% to 54.7% in the UV-vis spectra (Figs. 4a and 4b), and from 91.4% to 81.9% in the PL spectra, indicating a positive deuteration effect on the photostability of the compounds¹². Similar observations are found for the compounds doped in DPEPO film (Supplementary Fig. 43). To confirm the CT character in the absorption and emission bands, we perform in-situ EPR experiments and observe the generation of *N*-radicals in the TADF compounds in

powder form. Supplementary Fig. 44 shows the time-dependent EPR spectra of all compounds, where we observe the accumulation of long-lived radicals during irradiation, and a single spin signal with *g* value at 2.0030 that is consistent with the reported aminopyridine radical^{37,38}. To better understand the effect of deuterated emitters to the photostability under a host-guest environment, we also perform PL stability test of the TADF compounds doped in mCBP and the PL intensity drop over time is shown in Figs. 4c and 4d. Upon increasing the degree of deuteration, the percentage of the CT emission band drops from 69.1% to 56.4%, further confirming the important role of deuterated acceptors in addition to deuterated donors in the TADF compounds.

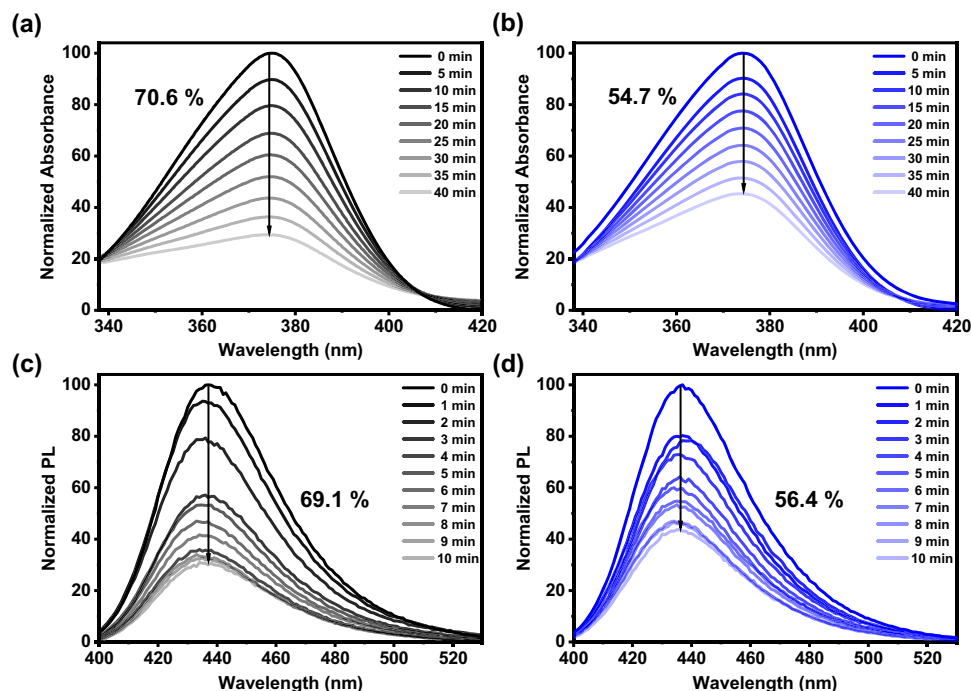


Fig. 4 | Photolysis results. UV-Vis spectra of (a) DPA-BO, (b) d-DPA-d-BO at 2×10^{-5} M in toluene solution over 40 min and PL spectra of 10 wt%, (c) DPA-BO, (d) d-DPA-d-BO doped in mCBP over 10 min under irradiation of 300 W xenon lamp.

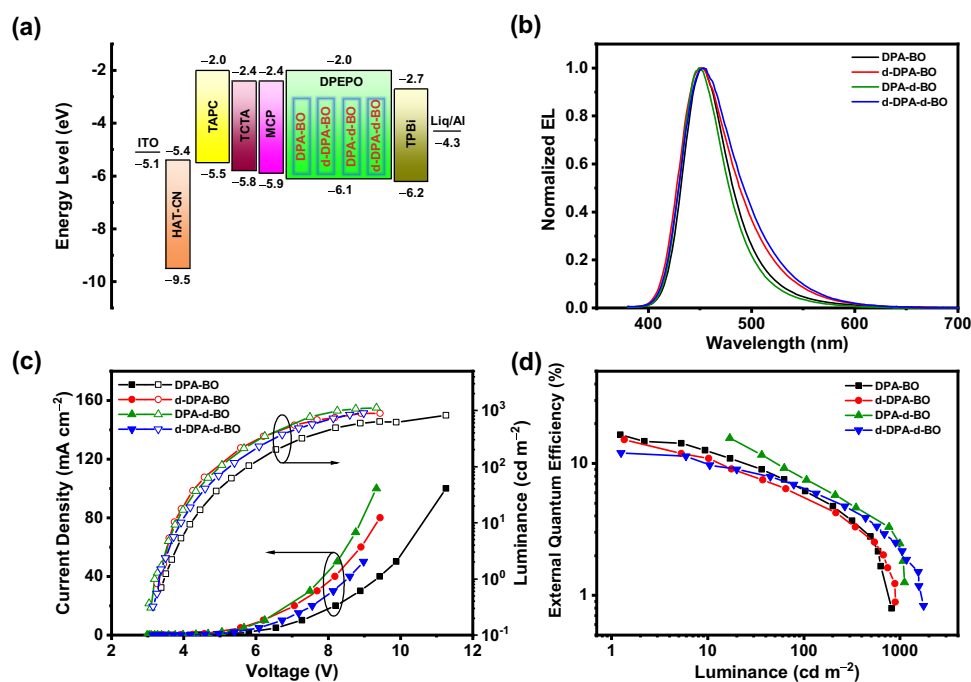


Fig. 5 | Device characteristics of the vacuum-deposited OLEDs based on 15 wt% of the compounds doped in DPEPO. a Device configuration and energy-level diagram. b Normalized EL spectra. c J - V - L plots. d EQE versus luminance.

Device characterization and correlation of intrinsic and operational stability

To confirm the TADF properties of the compounds, we fabricate a series of vacuum-deposited devices based on the dopant concentration of 5–20 wt% in DPEPO exhibiting blue EL. Figure 5 shows the device characteristics of 15 wt% of the compounds doped in DPEPO, while those of the others are shown in Supplementary Fig. 45 and summarized in Table 2. Apparently, these devices exhibit a blue EL

emission peak (λ_{EL}) at ca. 450 nm which corresponds to the CIE chromaticity coordinates of (0.15, 0.10). The high resemblance of the EL spectra to the corresponding PL spectra indicates a well confinement of excitons in the DPEPO host. As seen from the J - V - L device characteristics, the devices exhibit maximum EQEs of over 17%, further confirming the TADF properties of these compounds. Unfortunately, these devices exhibit limited operational lifetime, probably due to the close proximity of TADF molecules that lead to aggregated species and

Table 2 | Device characteristics of the vacuum-deposited OLEDs based on the TADF compounds doped in DPEPO

Compound	Conc. (wt%)	V_{on}^a (V)	L_{max}^b (cd m ⁻²)	λ_{max}^c (nm)	CIE ^d (x, y)	EQE _{max/100/1000} ^e (%)	$\Delta_{roll-off}^f$ (%)	CE ^g (cd A ⁻¹)	PE ^h (lm W ⁻¹)
DPA-BO	5	4.4	106	443	0.15, 0.08	11.6/1.3/-	88	5.3	3.7
	10	3.7	282	449	0.15, 0.09	13.4/4.1/-	70	8.0	5.9
	15	3.5	629	453	0.14, 0.11	16.5/6.2/-	54	12.4	11.1
	20	3.3	1361	454	0.14, 0.12	17.1/7.0/1.7	60	14.6	13.5
d-DPA-BO	5	4.1	138	439	0.16, 0.08	13.1/1.9/-	85	7.3	5.5
	10	3.6	342	446	0.15, 0.09	15.5/3.7/-	74	11.1	9.8
	15	3.3	890	450	0.15, 0.10	15.1/5.6/-	63	13.6	12.7
	20	3.2	1511	454	0.14, 0.11	14.6/6.1/2.1	59	14.0	13.7
DPA-d-BO	5	3.9	153	443	0.15, 0.08	12.4/3.2/-	76	4.2	2.8
	10	3.4	451	449	0.14, 0.09	14.1/5.9/-	60	6.8	5.0
	15	3.2	1111	450	0.14, 0.10	15.6/7.8/2.4	50	9.3	8.2
	20	3.2	1672	453	0.14, 0.11	14.8/8.6/3.5	42	9.4	7.6
d-DPA-d-BO	5	4.0	156	443	0.16, 0.07	13.5/2.1/-	85	7.2	5.4
	10	3.6	456	446	0.15, 0.09	15.4/4.3/-	77	11.3	9.9
	15	3.3	895	450	0.15, 0.10	16.3/6.0/-	64	14.8	13.8
	20	3.2	1758	454	0.15, 0.11	12.6/6.5/2.3	49	12.6	12.1

^a V_{on} represents turn-on voltage.

^b L_{max} represents maximum luminance.

^c λ_{max} represents peak maximum.

^dCIE coordinates are taken at luminance of 100 cd m⁻².

^eEQE_{max} represents maximum external quantum efficiency.

^fEfficiency roll-off measured by $\Delta_{roll-off} = 1 - (EQE_{100}/EQE_{max})$.

^gCE represents maximum current efficiency.

^hPE represents maximum power efficiency.

the relatively long excited-state lifetime in solid-state thin film, as evidenced above. In this regard, we turn to fabricate TADF-sensitized OLEDs to study the relationship between the molecular intrinsic stability, based on isotopic effect, and device operational stability. The device characteristics of vacuum-deposited TADF-sensitized OLEDs with *t*-Bu-*u*-DABNA³⁹ or BN3⁴⁰ as the emitter are illustrated in Fig. 6 and summarized in Table 3. These devices exhibit sharp EL bands peaking at ca. 461 nm or 572 nm, respectively, with maximum EQEs of over 20%. Notably, the device operational stability is found to follow the trend upon increasing the degree of deuteration of the TADF compounds, in which the LT₅₀ of the devices are found to be increased from ca. 20 h to 27 h at the luminance of 100 cd m⁻² for blue-emitting devices with CIE coordinates of (0.13, 0.09). It is worth mentioning that we observe a gradual increase in the LT₉₀ of the devices from ca. 12 h (DPA-BO), ca. 15 h (d-DPA-BO), ca. 19 h (DPA-d-BO) and ca. 23 h (d-DPA-d-BO) at the luminance of 1000 cd m⁻², which represent about 20-fold increase when compared to that based on BN3 only, i.e. 1.1 h. To have a better understanding of these enhancements, we further investigate the photolysis of the solid-state thin films of BN3 (10%) doped in mCBP, and BN3 (10%) with DPA-BO (15%) doped in mCBP (Supplementary Fig. 46). We observe an enhanced photostability in the presence of DPA-BO, with the reduced drop in the PL intensity from 62.0% (BN3) to 46.6% (BN3 with DPA-BO), as well as a reduced delayed lifetime (from 224.2 μ s to 196.3 μ s), possibly attributed to the accelerated RISC process. Finally, we also attempted to fabricate triplet-triplet upconversion (TTU) OLEDs based on this series of TADF compounds. The discussion of the EL characteristics for these OLEDs is included in Supplementary Note 1. The spatial localization of 3 wt% DPA-BO doped in 9-(1-naphthalenyl)-10-(4-(2-naphthalenyl)phenyl)anthracene (BH) is shown in Supplementary Fig. 47, while the EL characteristics are illustrated in Supplementary Fig. 48–50 and summarized in Supplementary Table 12–14; and the key performance of recently reported blue OLEDs with CIE_y ≤ 0.1 is listed in Supplementary Table 15. Considering the operational stability of the devices, similar observations have been found in the TTU OLEDs, demonstrating the versatility of the current approach to be applied to different types of devices.

Discussion

In conclusion, we present the subatomic modification of TADF emitters with targeted deuteration of donor and/or acceptor units and study the deuterated effect on their photophysical behavior, intrinsic stability and device operational stability. We found that the photostability of the deuterated isotopic analogues increases with the degree of deuteration, attributed to the higher intrinsic stability of the molecules with the increased number of deuterated substitutions through an additive effect of the multiple C–D bonds. We demonstrate that the deuteration of acceptor, in addition to a deuterated donor, is critical to boost the device lifetime of LT₉₀ from 15 h (deuterated donor only) to 23 h (deuterated donor and acceptor), an appreciable enhancement at the luminance of 1000 cd m⁻². Given the lack of sufficient attention on the effect of deuterated acceptors on enhancing the molecular stability across the field, we envisage that our present work provides insights and demonstrates the importance on modification of the chemical structures of materials at a subatomic level towards prolonging the device operational stability. Building upon our current study, we anticipate that such strategy could be applied to highly emissive narrowband multi-resonance TADF systems to fully harness the potential of these promising candidates for OLED applications.

Methods

Materials

2,5-dibromo-1,3-difluorobenzene, potassium carbonate, sodium tert-butoxide and tris(dibenzylideneacetone)dipalladium were purchased from Leyan. Phenol, Aniline-*d*₅ and bromobenzene-*d*₅ were purchased from Aladdin. Phenol-*d*₅, diphenylamine and boron tribromide were purchased from Sigma-Aldrich. Tri-tert-butylphosphine was purchased from Adamas. All solvents were purchased from General-Reagent. All commercially purchased chemicals were used without any further purification.

Characterization of the TADF Compounds

¹H and ¹³C{¹H} NMR spectra were recorded by Bruker Avance 400 (400 MHz for ¹H or 101 MHz for ¹³C{¹H} nuclei) Fourier-transform

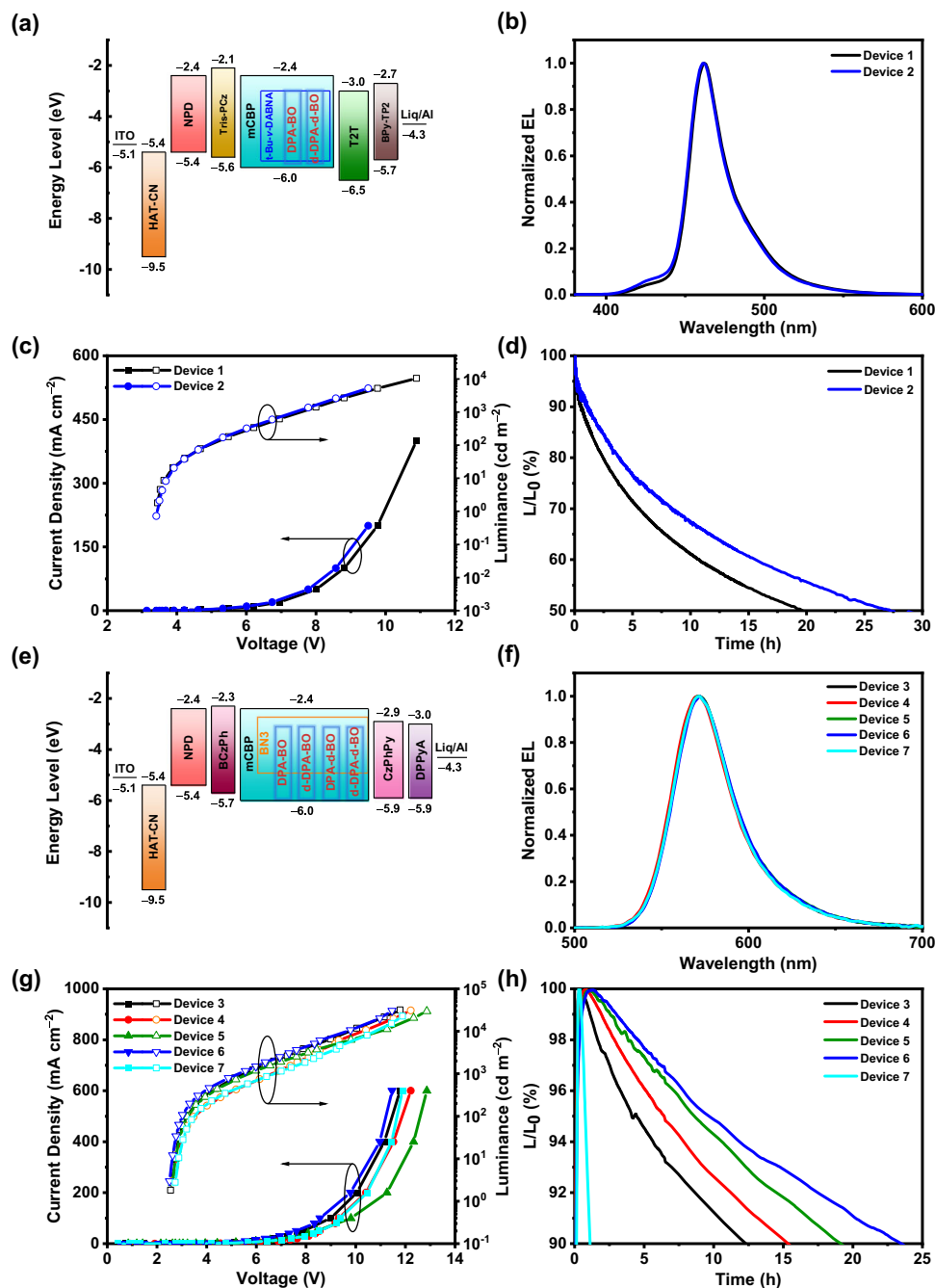


Fig. 6 | Device characteristics of the vacuum-deposited TADF-sensitized OLEDs.

a, e Device configuration and energy-level diagrams. **b, f** Normalized EL spectra. **c, g** I - V - L plots. **d, h** Operational lifetime projected at 1000 cd m^{-2} . Device 1 - t-Bu-*v*-DABNA (1 wt%) + DPA-BO (15 wt%), Device 2 - t-Bu-*v*-DABNA (1 wt%) + d-DPA-d-BO

(15 wt%), Device 3 - BN3 (10 wt%) + DPA-BO (15 wt%), Device 4 - BN3 (10 wt%) + d-DPA-BO (15 wt%), Device 5 - BN3 (10 wt%) + DPA-d-BO (15 wt%), Device 6 - BN3 (10 wt%) + d-DPA-d-BO (15 wt%), Device 7 - BN3 (10 wt%). All devices were doped in mCBP.

NMR spectrometer with chemical shifts reported relative to tetramethylsilane ($\delta = 0$ ppm) in chloroform and dimethyl sulfoxide. High resolution electrospray ionization (ESI) mass spectra were recorded by Thermo Scientific Exactive Benchtop LC/MS Orbitrap Mass Spectrometer. FT-IR spectra were measured by infrared spectrophotometer (Thermo Scientific Nicolet iS 50) from 4000 cm^{-1} to 400 cm^{-1} .

Absorption, emission spectra and PLQY measurements

The UV-vis absorption spectra were recorded by Cary 500 UV-vis (Agilent Technology) spectrophotometer equipped with a xenon flash lamp. Steady-state excitation and emission spectra were recorded by

Edinburgh Instruments Ltd FS5 spectrofluorometer. Delayed emission spectra were recorded by Edinburgh Instruments Ltd LP 980 transient absorption spectrometer. Liquid nitrogen was placed into Optistat DN (Oxford Instruments) for temperature-dependent measurements (77–298 K). Solid-state photophysical measurements were also performed for vacuum-deposited thin films inside Optistat DN. Excited-state lifetimes of solution and thin film of samples were measured in a conventional laser system. The excitation source was EPL-375 from Edinburgh Instruments which is a laser with wavelength ranging from 369 to 381 nm and output power (pulsed) of 0.11 to 0.15 mW. Luminescence decay signals were recorded by FLS 980 and analyzed by exponential fitting model. Absolute PLQYs in thin films were measured

Table 3 | Device characteristics of the vacuum-deposited TADF-sensitized OLEDs

Device	V_{on}^a (V)	L_{max}^b (cd m ⁻²)	λ_{max}^c (nm)	CIE ^d (x, y)	EQE _{max/100/1000} ^e (%)	$\Delta_{roll-off}^f$ (%)	CE ^g (cd A ⁻¹)	PE ^h (lm W ⁻¹)	LT ₉₀ ⁱ (h)	LT ₅₀ ⁱ (h)
1	3.4	10399	462	0.13, 0.10	5.1/4.2/3.4	33	4.6	4.1	-	19.7
2	3.4	10689	461	0.13, 0.09	5.0/4.2/3.4	32	4.3	3.8	-	27.3
3	2.5	31763	572	0.50, 0.50	19.5/14.2/3.8	81	70.4	80.2	12.3	-
4	2.6	30854	572	0.49, 0.50	20.9/12.8/3.4	84	75.1	82.9	15.4	-
5	2.6	29697	571	0.50, 0.50	16.5/13.1/3.5	79	59.9	64.8	19.1	-
6	2.5	30426	572	0.50, 0.50	18.5/15.1/3.6	81	67.7	76.9	23.4	-
7	2.7	22658	572	0.50, 0.50	15.2/10.2/2.2	86	56.3	58.0	1.1	-

^a V_{on} represents turn-on voltage.

^b L_{max} represents maximum luminance.

^c λ_{max} represents peak maximum.

^dCIE coordinates are taken at luminance of 100 cd m⁻².

^eEQE_{max} represents maximum external quantum efficiency.

^fEfficiency roll-off measured by $\Delta_{roll-off} = 1 - (EQE_{1000}/EQE_{max})$.

^gCE represents maximum current efficiency.

^hPE represents maximum power efficiency.

ⁱOperational lifetime projected at 1000 cd m⁻².

by Hamamatsu Quantaaurus-QY Absolute PL quantum yield spectrometer C11347-11.

Ultraviolet photoelectron spectroscopy

The UPS data were measured using X-ray photoelectron spectrometer (ThermoFischer, ESCALAB Xi⁺) under the operational vacuum pressure of 8×10^{-10} Pa and energy of power source of 21.22 eV (HeI excitation source). Operating voltage was 12.5 kV and the accumulated signal was obtained in 10 cycles.

Thermal analysis measurements

Thermogravimetric analysis was performed by Mettler TGA2 thermogravimeter where the sample weight losses were measured from 25 °C to 100 °C (kept at 15 min) then to 800 °C at a rate of 10 °C/min under nitrogen. Differential scanning calorimetry was carried out in SmartLab (Rigaku) by heating the samples from 50 °C to 350 °C at a rate 10 °C/min, followed by cooling process at the same rate. The samples were heated in two different cycles.

Photolysis measurements

2×10^{-5} M of each compound in toluene solution was added to a quartz cell with path length of 1.0 cm, whereas the compounds doped in mCBP thin film were prepared by vacuum evaporation system FS-450. They were photo-irradiated with broadband light by using a xenon lamp (300 W, CEL-PF300-T6). The UV-vis absorption and photoluminescence spectra were recorded during photolysis over time. The compounds in neat film were fabricated in vacuum evaporation system FS-450 and photo-irradiated with broadband light from 150 W ozone-free xenon arc lamp in Optistat DN.

Electron paramagnetic resonance

EPR measurements were performed with a Bruker A300 in nitrogen condition at room temperature. 5 mg of samples were weighed into the paramagnetic tube tested with light source 355 nm laser power 3 W light source model AO-L-355 and using solid 1,1-diphenyl-2-picrylhydrazyl as internal standard. A total of 12 data points of each sample was acquired in every 5 min for 1 h and 12 data points of selected samples were acquired every 30 min for 5 h.

Time-of-flight secondary ion mass spectrometry

The emissive layer was formed by co-depositing respective TADF compounds, DPEPO and BH at different concentrations, with the thickness of 200 nm. ToF-SIMS was carried out in Nano TOF 2 instrument (ULVAC-PHI, Japan) equipped with bismuth as the primary ion source as well as Ar/GCIB/Cs ion as sputter source. The ToF-

SIMS data was acquired on an area of $100 \times 100 \mu\text{m}^2$ by using 30 keV Bi primary ion beam, followed by a 3 s/cycle sputter of a $400 \times 400 \mu\text{m}^2$ area using 3 keV Ar ion beams. The sputter rate is 0.3 nm/s (Ar⁺) for SiO₂. The sample holder with samples was sealed in a container filled with Ar gas and transferred into the instrument immediately before testing.

Computational details

DFT and TDDFT calculations were carried out with the Gaussian 16 suite of programs⁴¹. By DFT, the ground-state (S_0) geometries of DPA-BO, d-DPA-BO, DPA-d-BO and d-DPA-d-BO were fully optimized in toluene with the hybrid Perdew, Burke, and Ernzerhof (PBE0) functional⁴²⁻⁴⁴, in conjugation with the polarization continuum model (PCM)⁴⁵⁻⁴⁷. TDDFT⁴⁸⁻⁵⁰ calculations at the same level associated with PCM were then carried out on the optimized S_0 geometries to compute the singlet-singlet transitions in the electronic absorption spectra of the compounds. Simulated absorption spectra of the compounds were generated by Multiwfn 3.8⁵¹. In order to gain insights into the excited states involved in thermally activated delayed fluorescence, the geometries of the lowest-lying singlet excited state (S_1), lowest-lying triplet excited state (T_1) and second lowest-lying triplet excited state (T_2) of the compounds were optimized using TDDFT with the PBE0 functional⁴²⁻⁴⁴. On the basis of the optimized geometries, vibrational frequencies were calculated and all stationary points were verified to be minima on the potential energy surface, as there were no imaginary frequencies observed (NIMAG = 0). The Cartesian coordinates of the optimized ground- and excited-state geometries are given in Supplementary Table 12–21. For all calculations, the 6-31 G(d,p) basis set⁵²⁻⁵⁴ was employed for all elements. A pruned (99,590) grid was used for numerical integration. Spin-orbit coupling (SOC) calculation was performed using the ORCA 5.0.3 program by quasi-degenerate perturbation theory from TDDFT²⁹. SOC matrices of all the compounds between the singlets and triplets were calculated and printed with B3LYP/def2-TZVP method in gas state, from which the total spin-orbit coupling matrix elements ($\langle S | \hat{H}_{SOC} | T \rangle$) were calculated^{55,56}. On the basis of the optimized S_0 geometries, the zero-point energies of the compounds and their respective donors and acceptors moieties were calculated using Multiwfn 3.8⁵¹, while the bond dissociation energies were calculated at the M06-2X/6-311++G(d,p) level⁵⁷. Based on the optimized S_0 and S_1 geometries, the displacement (ΔQ), Huang-Rhys factors (S_j) and reorganization energies (λ_j) of the normal modes of the compounds were calculated by the Molecular Materials Property Prediction Package (MOMAP)⁵⁸. In order to investigate the intermolecular interactions in the solid-state thin film, geometry optimization of the dimer of DPA-BO has been performed at the M06/6-31 G(d,p) level.

Device fabrication and characterization

DPEPO-based devices were prepared with the configuration of ITO/HATCN (10 nm)/TAPC (40 nm)/TCTA (10 nm)/MCP (10 nm)/*x* wt% TADF compounds:DPEPO (25 nm)/TPBi (40 nm)/Liq (1 nm)/Al (100 nm), in which HATCN, TAPC/TCTA, MCP, TPBi and Liq were used as hole-injection, hole-transporting, electron-blocking, electron-transporting and electron injection layers, respectively. The emissive layer was formed by co-depositing respective TADF compound and DPEPO at different concentrations. For TADF-sensitized OLEDs, devices were prepared with architectures of ITO/HATCN (10 nm)/NPD (40 nm)/Tris-PCz (10 nm)/1 wt% *t*-Bu-*ν*-DABNA:15 wt% TADF compounds:mCBP (25 nm)/T2T (10 nm)/BPy-TP2 (40 nm)/Liq (1 nm)/Al (100 nm) and ITO/HATCN (5 nm)/NPD (30 nm)/BCzPh (10 nm)/10 wt% BN3:15 wt% TADF compounds:mCBP (25 nm)/CzPhPy (10 nm)/DPPyA (30 nm)/Liq (1 nm)/Al (120 nm). For TTU OLEDs, devices were fabricated with the architecture of ITO/3 wt% *p*-dopant:HTL1 (10 nm)/HTL1 (50 nm)/HTL2 (5 nm)/emissive layer (20 nm)/ETL1 (5 nm)/50 wt% Liq:ETL2 (30 nm)/Liq (2 nm)/Al (120 nm), in which the emissive layer was built by co-depositing 3 wt% of respective TADF compound and BH host simultaneously. All OLEDs were fabricated on the pre-patterned ITO-coated glass substrates with sheet resistance of 15 Ω per square. The substrates were cleaned with Decon 90, rinsed with deionized water and ethanol, then dried in an oven, and finally treated in an ultraviolet ozone chamber for 20 min before loading into a vacuum evaporation system. The films were sequentially deposited at a rate of 0.1–0.2 nm s⁻¹ at a pressure of ca. 3 × 10⁻⁶ Torr without vacuum break. A shadow mask was used to define the pixel size of 0.09 cm². The thickness and deposition rate were monitored in situ during deposition by an oscillating quartz thickness monitor. Current density–voltage–luminance characteristics and EL spectra were measured with a Keithley 2400 semiconductor characterization system. The operational lifetime of the OLED devices was measured by a PR-OLEDLT-16 OLED aging tester.

Measurement of transient electroluminescence

Transient EL data were obtained using Tektronix AFG 1062 signal generator working under pulse mode, with 10 KHz repetition rate, 10% duty cycle, to excite the sample. The resulting EL signal was detected by Zolix OmniFluo990-H which integrated with sample chamber, monochromator, PMT (CRI31, response time 2.2 ns), and signal acquisition device DSC900PC.

Data availability

The data generated in this study are provided in the Supplementary Information. Source data are provided with this paper.

References

- Zhang, Y. & Forrest, S. R. Triplets contribute to both an increase and loss in fluorescent yield in organic light emitting diodes. *Phys. Rev. Lett.* **108**, 267404 (2012).
- Chung, W. J. & Lee, J. Y. Highly efficient and stable blue organic light-emitting diodes through the selective quenching of long-living triplet exciton of a thermally activated delayed fluorescence emitter. *J. Mater. Chem. C* **9**, 7458–7464 (2021).
- Zhang, Y., Lee, J. & Forrest, S. R. Tenfold increase in the lifetime of blue phosphorescent organic light-emitting diodes. *Nat. Commun.* **5**, 5008 (2014).
- Lee, J. et al. Hot excited state management for long-lived blue phosphorescent organic light-emitting diodes. *Nat. Commun.* **8**, 15566 (2017).
- Chan, C.-Y. et al. Stable pure-blue hyperfluorescence organic light-emitting diodes with high-efficiency and narrow emission. *Nat. Photon.* **15**, 203–207 (2021).
- Scholz, S., Kondakov, D., Lüssem, B. & Leo, K. Degradation mechanisms and reactions in organic light-emitting devices. *Chem. Rev.* **115**, 8449–8503 (2015).
- Jeon, S. O. et al. High-efficiency, long-lifetime deep-blue organic light-emitting diodes. *Nat. Photon.* **15**, 208–215 (2021).
- Zhang, D. & Duan, L. TADF sensitization targets deep-blue. *Nat. Photon.* **15**, 173–174 (2021).
- Sun, J. et al. Exceptionally stable blue phosphorescent organic light-emitting diodes. *Nat. Photon.* **16**, 212–218 (2022).
- Tsuji, H., Mitsui, C. & Nakamura, E. The hydrogen/deuterium isotope effect of the host material on the lifetime of organic light-emitting diodes. *Chem. Commun.* **50**, 14870–14872 (2014).
- Liu, X. et al. Isotope effect of host material on device stability of thermally activated delayed fluorescence organic light-emitting diodes. *Small Sci.* **1**, 2000057 (2021).
- Yao, J., Dong, S.-C., Tam, B. S. T. & Tang, C. W. Lifetime enhancement and degradation study of blue OLEDs using deuterated materials. *ACS Appl. Mater. Interfaces* **15**, 7255–7262 (2023).
- Wang, Y., Bai, F.-Q. & Zhang, H.-X. Intrinsic quantum efficiency enhancement in well-known Ir(III) complexes by virtue of a simple and controllable deuteration strategy. *Mater. Chem. Front.* **2**, 1215–1224 (2018).
- Bae, H. J. et al. Protecting benzylic C–H bonds by deuteration doubles the operational lifetime of deep-blue Ir-phenylimidazole dopants in phosphorescent OLEDs. *Adv. Opt. Mater.* **9**, 2100630 (2021).
- Li, W. et al. Improved efficiency and stability of red phosphorescent organic light-emitting diodes via selective deuteration. *J. Phys. Chem. Lett.* **13**, 1494–1499 (2022).
- Peng, X. et al. Near-infrared OLEDs based on functional pyrazinyl azolate Os(II) phosphors and deuteration. *Adv. Opt. Mater.* **10**, 2201291 (2022).
- Wang, S.-F. et al. Polyatomic molecules with emission quantum yields >20% enable efficient organic light-emitting diodes in the NIR(II) window. *Nat. Photon.* **16**, 843–850 (2022).
- Wang, P. et al. Synthesis of all-deuterated tris(2-phenylpyridine)iridium for highly stable electrophosphorescence: the “deuterium effect”. *J. Mater. Chem. C* **1**, 4821–4825 (2013).
- Huang, T. et al. Boosting the efficiency and stability of blue TADF emitters by deuteration. *ChemRxiv* (2021).
- Cheng, J.-F. et al. Positive isotope effect in thermally activated delayed fluorescence emitters based on deuterium-substituted donor units. *Chem. Eng. J.* **430**, 132822 (2022).
- Singh, K. & Blümich, B. Online monitoring of the kinetic isotope effect in chemical reactions with ¹H and ¹⁹F low-field NMR spectroscopy. *Analyst* **143**, 4408–4421 (2018).
- Singleton, D. A. et al. ¹³C Kinetic isotope effects and the mechanism of the uncatalyzed decarboxylation of orotic acid. *J. Am. Chem. Soc.* **122**, 3296–3300 (2000).
- Shao, M. et al. The isotopic effects of deuteration on optoelectronic properties of conducting polymers. *Nat. Commun.* **5**, 3180 (2014).
- Liu, X. et al. Isotope effect in the magneto-optoelectronic response of organic light-emitting diodes based on donor–acceptor exciplexes. *Adv. Mater.* **32**, 2004421 (2020).
- Ko, S.-B., Kang, S. & Kim, T. A silane-based bipolar host with high triplet energy for high efficiency deep-blue phosphorescent OLEDs with improved device lifetime. *Chem. Eur. J.* **26**, 7767–7773 (2020).
- Nagamura, N. et al. A multifunctional hole-transporter for high-performance TADF OLEDs and clarification of factors governing the transport property by multiscale simulation. *J. Mater. Chem. C* **10**, 8694–8701 (2022).
- Ahn, D. H. et al. Highly efficient blue thermally activated delayed fluorescence emitters based on symmetrical and rigid oxygen-bridged boron acceptors. *Nat. Photon.* **13**, 540–546 (2019).
- Kim, J. U. et al. Nanosecond-time-scale delayed fluorescence molecule for deep-blue OLEDs with small efficiency rolloff. *Nat. Commun.* **11**, 1765 (2020).
- Neese, F. Software update: The ORCA program system—Version 5.0. *WIREs Comput. Mol. Sci.* **12**, e1606 (2022).

30. Moraes, I. R. D., Scholz, S., Lüssem, B. & Leo, K. Analysis of chemical degradation mechanism within sky blue phosphorescent organic light emitting diodes by laser-desorption/ionization time-of-flight mass spectrometry. *Org. Electron.* **12**, 341–347 (2011).
31. Thanh Dang, T. et al. Experimental and computational studies of deuterated ethanols: gas-phase acidities, electron affinities and bond dissociation energies. *Int. J. Mass Spectrom. Ion Processes* **123**, 171–185 (1993).
32. Choi, H., Ogi, S., Ando, N. & Yamaguchi, S. Dual trapping of a metastable planarized triarylborane π -system based on folding and lewis acid–base complexation for seeded polymerization. *J. Am. Chem. Soc.* **143**, 2953–2961 (2021).
33. Guo, J., Yang, Y., Dou, C. & Wang, Y. Boron-containing organic diradicaloids: dynamically modulating singlet diradical character by Lewis acid–base coordination. *J. Am. Chem. Soc.* **143**, 18272–18279 (2021).
34. Li, L.-K. et al. Strategies towards rational design of gold(III) complexes for high-performance organic light-emitting devices. *Nat. Photon.* **13**, 185–191 (2019).
35. Cui, L.-S. et al. Fast spin-flip enables efficient and stable organic electroluminescence from charge-transfer states. *Nat. Photon.* **14**, 636–642 (2020).
36. Drummond, B. H. et al. Electron spin resonance resolves intermediate triplet states in delayed fluorescence. *Nat. Commun.* **12**, 4532 (2021).
37. Neugebauer, F. A., Fischer, H., Bamberger, S. & Smith, H. O. Aminyle, 6. tert-butyl-substituierte 9-carbazolyl-radikale, carbazol-radikalkationen und carbazol-9-oxyl-radikale. *Chem. Ber.* **105**, 2694–2713 (1972).
38. Kondakov, D. Y., Pawlik, T. D., Nichols, W. F. & Lenhart, W. C. Free-radical pathways in operational degradation of OLEDs. *J. Soc. Inf. Disp.* **16**, 37–46 (2008).
39. Naveen, K. R. et al. Achieving high efficiency and pure blue color in hyperfluorescence organic light emitting diodes using organoboron based emitters. *Adv. Funct. Mater.* **32**, 2110356 (2022).
40. Qi, Y. et al. Peripheral decoration of multi-resonance molecules as a versatile approach for simultaneous long-wavelength and narrow-band emission. *Adv. Funct. Mater.* **31**, 2102017 (2021).
41. Frisch, M. J. et al. Gaussian 16, Revision A.03. (Gaussian, Inc., Wallingford CT, 2016).
42. Perdew, J. P., Burke, K. & Ernzerhof, M. Generalized gradient approximation made simple. *Phys. Rev. Lett.* **77**, 3865–3868 (1996).
43. Perdew, J. P., Burke, K. & Ernzerhof, M. Generalized gradient approximation made simple. *Phys. Rev. Lett.* **78**, 1396–1396 (1997).
44. Adamo, C. & Barone, V. Toward reliable density functional methods without adjustable parameters: The PBE0 model. *J. Chem. Phys.* **110**, 6158–6170 (1999).
45. Miertuš, S., Scrocco, E. & Tomasi, J. Electrostatic interaction of a solute with a continuum. A direct utilization of AB initio molecular potentials for the prevision of solvent effects. *Chem. Phys.* **55**, 117–129 (1981).
46. Miertuš, S. & Tomasi, J. Approximate evaluations of the electrostatic free energy and internal energy changes in solution processes. *Chem. Phys.* **65**, 239–245 (1982).
47. Pascual-ahuir, J. L., Silla, E. & Tuñón, I. GEPOL: An improved description of molecular surfaces. III. A new algorithm for the computation of a solvent-excluding surface. *J. Comput. Chem.* **15**, 1127–1138 (1994).
48. Bauernschmitt, R. & Ahlrichs, R. Treatment of electronic excitations within the adiabatic approximation of time dependent density functional theory. *Chem. Phys. Lett.* **256**, 454–464 (1996).
49. Casida, M. E., Jamorski, C., Casida, K. C. & Salahub, D. R. Molecular excitation energies to high-lying bound states from time-dependent density-functional response theory: Characterization and correction of the time-dependent local density approximation ionization threshold. *J. Chem. Phys.* **108**, 4439–4449 (1998).
50. Stratmann, R. E., Scuseria, G. E. & Frisch, M. J. An efficient implementation of time-dependent density-functional theory for the calculation of excitation energies of large molecules. *J. Chem. Phys.* **109**, 8218–8224 (1998).
51. Lu, T. & Chen, F. Multiwfn: a multifunctional wavefunction analyzer. *J. Comput. Chem.* **33**, 580–592 (2012).
52. Hehre, W. J., Ditchfield, R. & Pople, J. A. Self-consistent molecular orbital methods. XII. Further extensions of Gaussian-type basis sets for use in molecular orbital studies of organic molecules. *J. Chem. Phys.* **56**, 2257–2261 (1972).
53. Hariharan, P. C. & Pople, J. A. The influence of polarization functions on molecular orbital hydrogenation energies. *Theoret. Chim. Acta* **28**, 213–222 (1973).
54. Francl, M. M. et al. Self-consistent molecular orbital methods. XXIII. A polarization-type basis set for second-row elements. *J. Chem. Phys.* **77**, 3654–3665 (1982).
55. Stephens, P. J., Devlin, F. J., Chabalowski, C. F. & Frisch, M. J. Ab initio calculation of vibrational absorption and circular dichroism spectra using density functional force fields. *J. Phys. Chem.* **98**, 11623–11627 (1994).
56. Weigend, F. & Ahlrichs, R. Balanced basis sets of split valence, triple zeta valence and quadruple zeta valence quality for H to Rn: Design and assessment of accuracy. *Phys. Chem. Chem. Phys.* **7**, 3297–3305 (2005).
57. Zhao, Y. & Truhlar, D. G. The M06 suite of density functionals for main group thermochemistry, thermochemical kinetics, non-covalent interactions, excited states, and transition elements: two new functionals and systematic testing of four M06-class functionals and 12 other functionals. *Theor. Chem. Acc.* **120**, 215–241 (2008).
58. Shuai, Z. Thermal vibration correlation function formalism for molecular excited state decay rates. *Chin. J. Chem.* **38**, 1223–1232 (2020).
59. Yang, Z. et al. A sterically hindered asymmetric D-A-D' thermally activated delayed fluorescence emitter for highly efficient non-doped organic light-emitting diodes. *Chem. Sci.* **10**, 8129–8134 (2019).

Acknowledgements

The work described in this paper was fully supported by a grant from the National Natural Science Foundation of China (Project No. 22275114), Science and Technology Planning Project of Shenzhen Municipality (Grant number: WDZC20220817160017003; WDZC20220810152404001), Cross-Disciplinary Research Fund of Tsinghua Shenzhen International Graduate School (SIGS), Tsinghua University (Grant number: JC2022003), Overseas Research Cooperation Fund Research Plan of Tsinghua SIGS (Grant number: HW2023006) and Scientific Research Startup Fund of SIGS, Tsinghua University (Grant numbers: QD2021027C and QD2023001C). W.-L.C. acknowledges the receipt of postgraduate studentships from the Science and Technology Planning Project of Shenzhen Municipality. The computations were performed using the SIGS research computing facilities.

Author contributions

M.-C.T. initiated and designed the research. M.-C.T. and S.J. designed the TADF compounds. M.-C.T., S.J., C.W., and X.S. conducted the synthesis, characterization, and photophysical measurements of the compounds. W.-L.C., W.L., and W.C. carried out the OLED fabrication and characterizations. S.L., M.W., M.N., and W.K.T. performed and analyzed the computational calculations. M.-C.T., G.W., S.S.C., and Q.S. supervised the work. All authors discussed the results and contributed to the manuscript.

Competing interests

The authors declare no competing interests.

Additional information

Supplementary information The online version contains supplementary material available at <https://doi.org/10.1038/s41467-023-42019-6>.

Correspondence and requests for materials should be addressed to Guodan Wei, Season Si Chen or Man-Chung Tang.

Peer review information *Nature Communications* thanks the anonymous reviewer(s) for their contribution to the peer review of this work. A peer review file is available.

Reprints and permissions information is available at <http://www.nature.com/reprints>

Publisher's note Springer Nature remains neutral with regard to jurisdictional claims in published maps and institutional affiliations.

Open Access This article is licensed under a Creative Commons Attribution 4.0 International License, which permits use, sharing, adaptation, distribution and reproduction in any medium or format, as long as you give appropriate credit to the original author(s) and the source, provide a link to the Creative Commons license, and indicate if changes were made. The images or other third party material in this article are included in the article's Creative Commons license, unless indicated otherwise in a credit line to the material. If material is not included in the article's Creative Commons license and your intended use is not permitted by statutory regulation or exceeds the permitted use, you will need to obtain permission directly from the copyright holder. To view a copy of this license, visit <http://creativecommons.org/licenses/by/4.0/>.

© The Author(s) 2023, corrected publication 2023